Standard Model is best model (working title)

William Kennedy DiClemente

A DISSERTATION

in

Physics and Astronomy

Presented to the Faculties of The University of Pennsylvania

in Partial Fulfillment of the Requirements for the Degree of Doctor of Philosophy

2018 Last compiled: December 29, 2018

I. Joseph Kroll, Professor, Physics

Supervisor of Dissertation

Joshua Klein, Professor, Physics

Graduate Group Chairperson

<u>Dissertation Committee</u>

(Committee Prof. 1), Professor, Physics

(Committee Prof. 2), Associate Professor, Physics

(Committee Prof. 3), Professor, Physics

(Committee Prof. 4), Professor, Physics

I. Joseph Kroll, Professor, Physics

Standard Model is best model (working title)

Acknowledgements

I'd like to thanks the Ghosts of Penn Students Past for providing me with such an amazing thesis template.

ABSTRACT

STANDARD MODEL IS BEST MODEL (WORKING TITLE)

William Kennedy DiClemente

J. Kroll

This is the abstract text.

Contents

List of Tables

List of Figures

Preface

This is the preface. It's optional, but it's nice to give some context for the reader and stuff.

Will K. DiClemente
Philadelphia, February 2019

Chapter 1

Introduction

The Standard Model (SM)[1] has been remarkably successful...

[1] Here's a footnote.

Chapter 2

Theoretical Framework

(Some example introductory text for this chapter)...

2.1 Introduction to the Standard Model

Modern particle physics is generally interpreted in terms of the Standard Model (SM). This is a quantum field theory which encapsulates our understanding of the electromagnetic, weak, and strong interactions...

2.2 Electroweak Mixing and the Higgs Field

When the theory of the electroweak interaction was first developed [2, 3], the W and Z bosons were predicted to be massless (a typical mass term in the Lagrangian would violate the SU(2) symmetry). However, these were experimentally observed to have masses...

Chapter 3

LHC and the ATLAS Detector

3.1 The Large Hadron Collider

The Large Hadron Collider (LHC) [4] is...

3.2 The ATLAS Detector

ATLAS is a general-purpose particle detector...

3.2.1 The Inner Detector

The Inner Detector serves the primary purpose of measuring the trajectories of charged particles...

3.2.1.1 Pixel Detector

The Pixel detector consists of four cylindrical barrel layers and three disk-shaped endcap layers...

3.2.1.2 Semiconductor Tracker

The Semiconductor Tracker uses the same basic technology as the Pixels, but the fundamental unit of silicon is a larger "strip"...

3.2.1.3 Transition Radiation Tracker

The Transition Radiation Tracker is the outermost component of the ID...

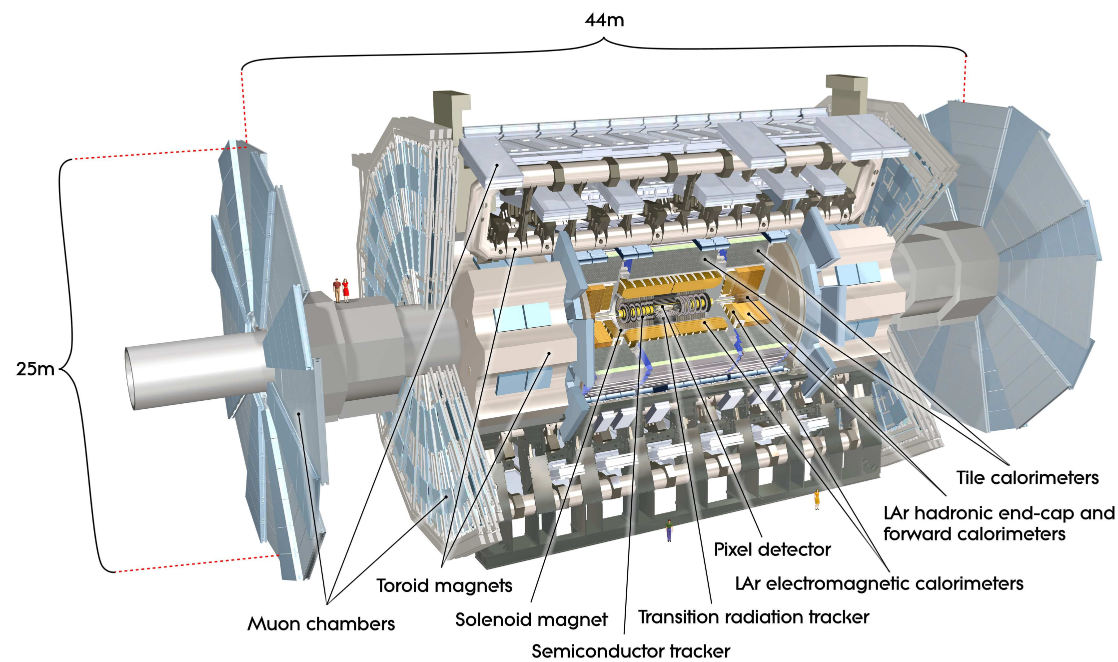

Figure 3.1: General cut-away view of the ATLAS detector [5].

3.2.2 The Calorimeters

ATLAS includes two types of calorimeter system for measuring electromagnetic and hadronic showers. These are the Liquid Argon (LAr) calorimeters and the Tile calorimeters. Together, these cover the region with $|\eta| < 4.9$...

3.2.2.1 Liquid Argon Calorimeters

The Liquid Argon system consists of...

3.2.2.2 Tile Calorimeters

The Tile calorimeter provides coverage for hadronic showers...

Chapter 4

Alignment of the ATLAS Inner Detector

In order for the subdetectors of the ID to operate at their designed precisions, it is essential that the locations of the sensors be known as precisely as possible. Differences between the expected and actual positions of a sensor can result in displaced particle hits and degrade track reconstruction quality. These misalignments can occur for any number of reasons, including but not limited to elemnts shifting during maintenance periods or cycles in ATLAS's magnetic field, or simply small movements during normal detector operations. Since it is not practical to physically realign hundreds of thousands of detector elements to μm precision by hand, an iterative track-based alignment algorithm is used to determine the physical positions and orientations of these elements [6]. The effects of misalignments and the steps taken to correct and monitor them are detailed in this chapter.

4.1 Effects of Misalignment

Hello world!

4.2 The Alignment Method

Hello world!

4.3 Momentum Bias Corrections

Hello world!

4.4 Alignment of the IBL

Hello world!

4.5 Alignment Monitoring

Hello world!

Chapter 5

WZ production @ $\sqrt{s} = 13$ TeV

5.1 Theoretical motivation

Hello world!

5.2 Signal definition

Hello world!

5.3 Background estimations

Hello world!

5.4 Cross section measurement

Hello world!

Chapter 6

Same-sign WW @ $\sqrt{s} = 13$ TeV

6.1 Theoretical motivation

Hello world!

6.2 Signal definition

Hello world!

6.3 Background estimations

Hello world!

6.4 Cross section measurement

Hello world!

Chapter 7

Prospects for same-sign WW at the High Luminosity LHC

On December 3, 2018, Run 2 of the LHC officialy ended, and the collider was shut down to begin the first of two scheduled extended maintenance periods [7]. During these two long shutdowns, the Phase-I and Phase-II upgrades of the LHC and ATLAS will occur in order to prepare for the High-Luminosity LHC (HL-LHC) which is scheduled to begin operation in 2026 [8].

The HL-LHC is planned to run at a center-of-mass energy of $\sqrt{s} = 14$ TeV with an instantaneous luminosity of $\mathcal{L} = 5 \times 10^{34}$ cm^{-2}s^{-1} corresponding to an average of 140 collisions per beam-crossing. Over the course of operation, the HL-LHC is expected to collect a total integrated luminosity of $\mathcal{L} = 3000$ fb^{-1} by 2035 [9].

These run conditions are much harsher than what ATLAS has experienced so far, and as a result there are several planned upgrades to the detector. Most notably, the entire ID will be replaced with an all-silicon tracker which will extend the coverage from $|\eta| \leq 2.7$ up to $|\eta| \leq 4.0$. This will allow for reconstruction of charged particle tracks which can in turn be matched to clusters in the calorimeters for electron identification or forward jet tagging [10].

The upgraded detector combined with the higher beam energy and the considerable increase in integrated luminosity means that many analyses with low signal statistics in Run 2 have the potential to be greatly improved with the HL-LHC. While the ATLAS 13 TeV $W^{\pm}W^{\pm}jj$ cross section measurement certainly did not suffer greatly from low statistics TODO: –reword–, the accuracy of the measurement can still be improved at the HL-LHC. Of particular interest is the longitudinal polarization of the W bosons due to its sensitivity to electroweak symmetry breaking [11].

The analysis detailed in this chapter is based off of the 2018 public ATLAS $W^{\pm}W^{\pm}jj$ prospects study [12] which is itself an extension of the 2017 ATLAS study [13]. TODO: mention CMS's study + yellow report?

7.0.1 Analysis Overview

The experimental signature of interest here is identical to the 13 TeV analysis detailed in Chapter 6: two prompt leptons (electrons or muons) with the same charge, missing transverse energy, and two jets. Once again the two leading jets are required to have a large angular separation and a high combined invariant mass to preferentially select EWK VBS production over QCD $W^{\pm}W^{\pm}jj$ events.

Background processes that can mimic the signal are again similar to the 13 TeV analysis. The dominant source of prompt background from WZ+jets events where both bosons decay leptonically. If the lepton from the Z-decay with opposite charge from the W falls outside of the detector acceptance or is not identified, the remainder could appear to be a $W^{\pm}W^{\pm}jj$ signal event. To a lesser extent, ZZ+jets events can enter the signal region in much the same way provided two leptons are "lost". Other prompt sources include $t\bar{t} + V$ and and multiple parton interactions, however these processes do not contribute much. The upgrades to the ATLAS detector are expected to reduce the size of these prompt contributions due in large part to the increased detector acceptance from the forward tracking. Jets mis-reconstructed as leptons or leptons from hacronic decays (such as $t\bar{t}$ and W+jets production) comprise the non-prompt lepton background. Lastly, events with two prompt, opposite-charge electrons can contribute provided one of the electrons is mis-reconstructed as the wrong charge.

In this analysis, the EWK production of $W^{\pm}W^{\pm}jj$ is studied in the context of the planned HL-LHC run conditions and upgraded ATLAS detector. An optimized event selection (referred to as the *optimized selection*) is also explored in an effort to gain increased signal significance over the *default selection*. The cross section of the inclusive EWK production is measured for both the default and optimized selections, and the extraction of the longitudinal scattering significance is measured with the optimized selection.

7.1 Theoretical motivation

The theoretical motivation for studying the ssWW process is detailed in Section 6.1. The particular interest in polarization is the potential for the scattering amplitude of longitudinally polarized weak bosons to diverge linearly as the center of mass energy increases, ultimately violating unitarity around 1 TeV [14]. In the Standard Model, the Higgs boson cancels these divergences. However, as the Higgs is recently discovered it is still extremely to study the mechanism of electroweak symmetry breaking (EWSB), and the longitudinal scattering of W bosons is expected to be one of the most sensitive tests of EWSB [11].

7.1.1 Experimental sensitivity to longitudinal polarization

There are three possible polarization states for a massive vector boson: two transverse ($+$ or $-$) and one longitudinal (0). Therefore, in a system with two W bosons, the overall polarization can be purely longitudinal (00), purely transverse ($++$, $--$, and $+-$), or mixed ($+0$ and -0). The three combinations will be referred to as LL, TT, and LT respectively.

In order extract the longitudinal scattering component, it is necessary to find variables that distinguish the LL from the TT and LT. Several variables were studied, and those with the best discriminating power between the polarizations were the leading and subleading lepton p_{T} (Figure 7.1) as well as the azimuthal separation of the two VBS jets (Figure 7.2). Ultimately, the extraction of the longitudinal scattering significance was performed using a binned likelihood fit to $|\Delta\phi_{jj}|$.

7.2 Monte Carlo samples

As no real HL-LHC data will be available for many years, all processes in this prospects study must be simulated using Monte Carlo (MC) generators. Signal and background processes were generated at $\sqrt{s} = 14$ TeV, and the event yields scaled to the anticipated HL-LHC integrated luminosity of $\mathcal{L} = 3000$ fb^{-1}.

TODO: Consider putting all this in a table

The signal sample consists of both VBS and non-VBS electroweak (EWK) $W^{\pm}W^{\pm}jj$ production, and it is sumulated with the `Madgraph5_aMC@NLO` generator [15] using the `NNPDF3.0` PDF set [16] and interfaced with `PYTHIA v8` [17] for hadronization and parton showering. To study the longitudinal polarization more directly, two additional `Madgraph5_aMC@NLO` $W^{\pm}W^{\pm}jj$ samples are used: one containing only the longitudinal contribution (LL) and a second containing the transverse (TT) and mixed (LT) contributions.

TODO: Here we talk about things that mimic the experimental signature before we formally state what the signal is... There are many other processes that can produce the same final state as the $W^{\pm}W^{\pm}jj$ and must also be accounted for using MC simulations. WZ events are generated using `SHERPA v2.2.0` [18, 19, 20], which includes up to one parton at next-to-leading order (NLO) in the strong coupling constant α_s and up to three additional partons at leading order (LO). Both EWK

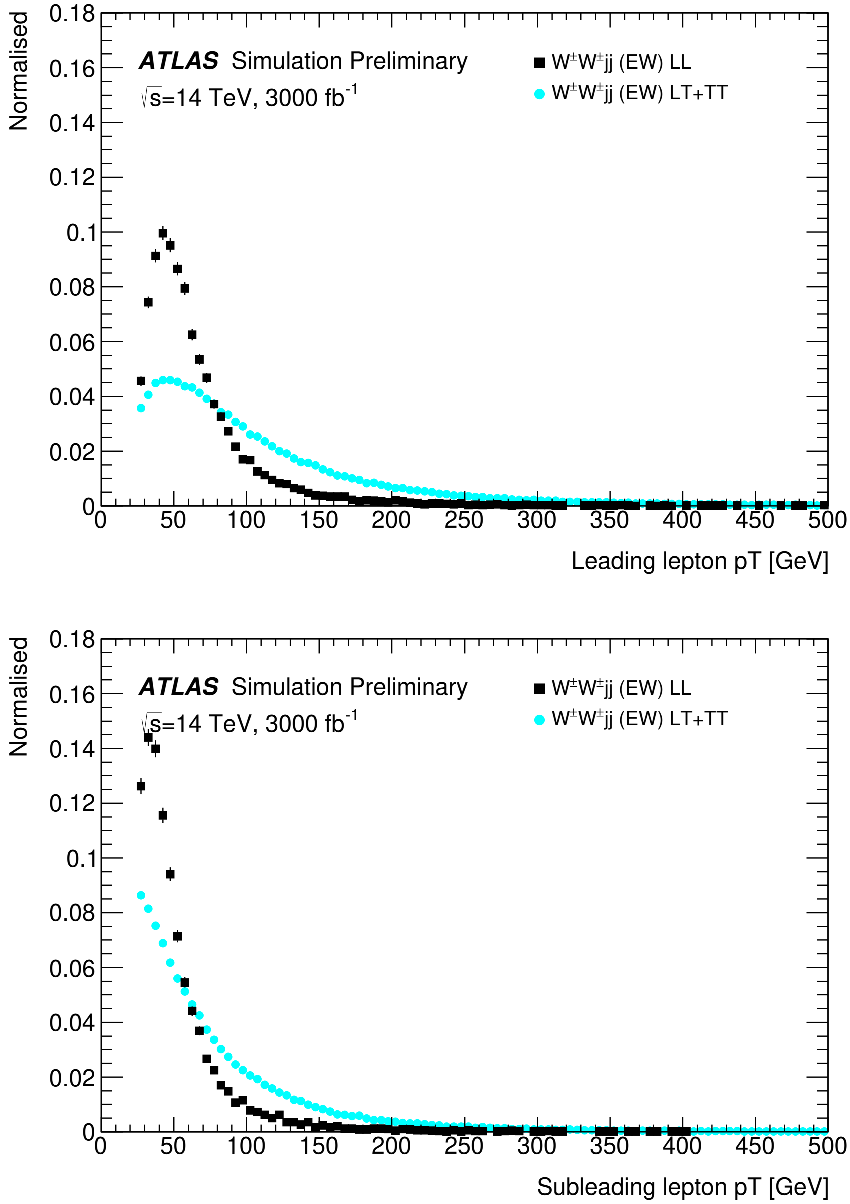

Figure 7.1: Comparison of the leading (top) and subleading (bottom) lepton p_{T} distributions for purely longitudinal (LL, black) and mixed polarization (LT+TT, cyan) $W^{\pm}W^{\pm}jj$ events. Plots from [1].

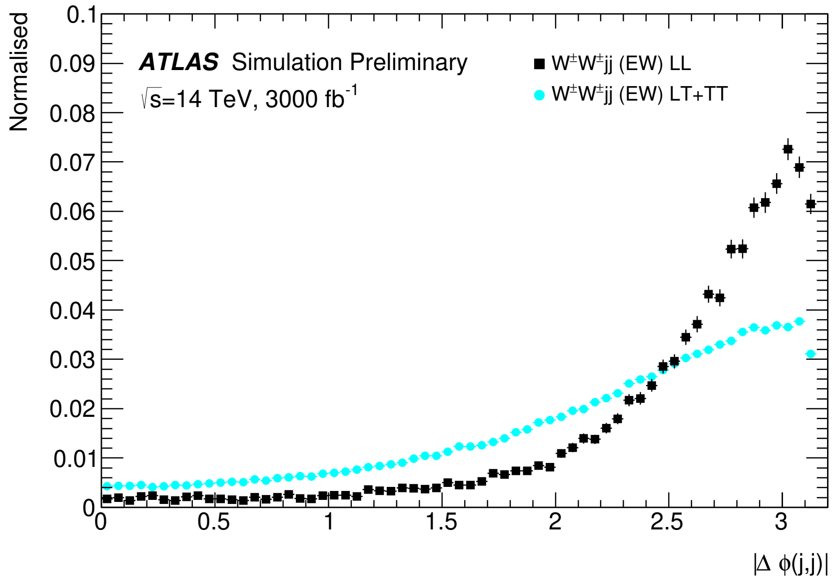

Figure 7.2: Comparison of the azimuthal dijet separation ($|\Delta\phi_{jj}|$) for purely longitudinal (LL, black) and mixed polarization (LT+TT, cyan) $W^{\pm}W^{\pm}jj$ events. Plot from [1].

and QCD production are included in these samples. ZZ events are generated using `SHERPA v2.2.2` with up to two additional partons in the final state. Triboson backgrounds $VVV, V = W, Z$ where the bosons can decay leptonically or hadronically are simulated with `SHERPA v2.2.2` with up to two additional partons in the final state. W+jets backgrounds are generated for electron, muon, and tau final states are generated at LO with `Madgraph5_aMC@NLO` and the `NNPDF3.0` set with showering from `PYTHIA v8` . Z+jets events are generated using `POWHEG-BOX` [21] and the `CT10` PDF set [22] interfaced with `PYTHIA v8` . Finally, $t\bar{t}$ and single-top events are generated using `POWHEG-BOX` with showering from `PYTHIA v6` .

Since the MC samples used in the analysis are generated at particle-level and have not been run through the typical full simulation of the ATLAS detector, smearing functions are instead used to estimate detector effects. These are derived from a `GEANT4` simulation of the detector [23].

7.3 Background estimations

TODO: MC samples, what we estimate directly from MC, Charge flip, fakes, and isolation

7.3.1 Truth based isolation

7.4 Event selection

TODO: Add table for full lepton (pre-)selection, full jet (pre-)selection, and then finally the overall event selection

The impact of the forward tracking on the lepton and jet selection was studied previously in [13] and the results are used here.

Selection requirement	Selection value
Lepton kinematics	$p_{\mathrm{T}} > 25$ GeV
	$\|\eta\| \leq 4.0$
Jet kinematics	$p_{\mathrm{T}} > 30$ GeV for $\|\eta\| \leq 4.5$
	$p_{\mathrm{T}} > 70$ GeV for $\|\eta\| > 3.8$
Dilepton charge	Exactly two signal leptons with same charge
Dilepton separation	$\Delta R_{l,l} \geq 0.3$
Dilepton mass	$m_{ll} > 20$ GeV
Z boson veto	$\|m_{ee} - m_Z\| > 10$ GeV (ee-channel only)
$E_{\mathrm{T}}^{\mathrm{miss}}$	$E_{\mathrm{T}}^{\mathrm{miss}} > 40$ GeV
Jet selection	At least two jets with $\Delta R_{l,j} > 0.3$
b jet veto	$N_{\text{b-jet}} = 0$
Dijet separation	$\Delta\eta_{jj} > 2.5$
Trilepton veto	No additional preselected leptons
Dijet mass	$m_{jj} > 500$ GeV
Lepton-jet centrality[2]	$\zeta > 0$

Table 7.1: derp

7.5 Selection optimization

As mentioned earlier, the HL-LHC will feature forward tracking, an increase in center of mass energy, and a higher integrated luminosity. Therefore, this study is an excellent time to see if there are new optimizations to the signal event selection that can improve the signal to background ratio.

7.5.1 Random grid search algorithm

The chosen method for optimizing the event selection is a cut-based algorithm known as the Random Grid Search (RGS) [24]. Consider a simple case of two variables x and y chosen to differentiate the signal from the background. In order to be considered a signal event, a given event would be required to pass a *cut point* $c = \{x > x_c, y > y_c\}$. A simple method to choose the optimal cut point (i.e. the "best" values of the cuts x_c and y_c) would be to construct an $n \times m$ rectangular grid in x and y consisting of points $(x_0, y_0), (x_1, y_1), ..., (x_n, y_m)$, as in Figure 7.3. One can then choose a cut point $c_k = \{x > x_i, y > y_j\}$ that maximizes the signal significance as measured by a chosen metric. This would be considered a *regular* or *rectangular* grid search.

While effective in principle, this rectangular grid search comes with two major drawbacks:

1. The algorithm does not scale well as the number of variables to be optimized–the dimensionality of the grid–increases. In the case of a square grid with N bins per variable v, the number of cut points to be evaluated grows as N^v.

2. Signal and background samples are rarely evenly distributed over the entire grid, resulting in many cut points being sub-optimal and evaluating them would be a waste of computing resources.

To combat these limitations, the RGS algorithm constructs a grid of cut points directly from the signal sample itself. In the two-dimensional example, this means that the variables x_i and y_j making up the cut point $c_k = \{x > x_i, y > y_j\}$ take their values directly from a given signal event. This has the benefit of creating a *random grid* of cut points that is by construction biased towards regions of high signal concentration. This reduces the need for exponentially increasing numbers of cut points while ensuring that computing resources are not wasted in regions with few to no signal events. An example of the the two-dimensional random grid is shown in Figure 7.4.

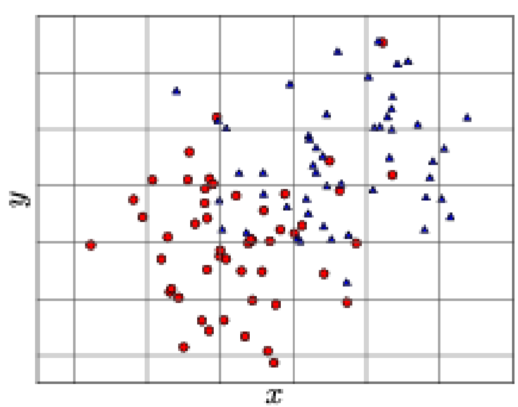

Figure 7.3: A visual representation of a rectangular grid search algorithm. The signal events are the blue triangles, and the red circles are the background events. TODO: replace with own figure

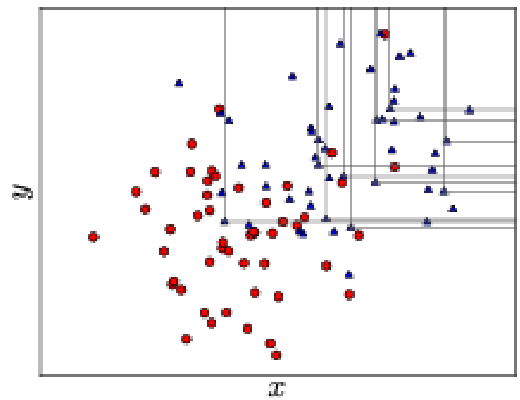

Figure 7.4: A visual representation of a random grid search algorithm. The signal events are the blue triangles, and the red circles are the background events. TODO: replace with own figure

Once the random grid of cut points is constructed, the optimal cut point can be chosen using whatever metric the analyzer chooses, such as signal to background ratio. For the purpose of the $W^{\pm}W^{\pm}jj$ upgrade study, the optimal cut point is the one that mazimizes the signal significance Z defined as in Equation 7.1 [25].

$$Z = \sqrt{2\left[(s+b)\ln\left(\frac{s+b}{b_0}\right) + b_0 - s - b\right] + \frac{(b-b_0)^2}{\sigma_b^2}} \tag{7.1}$$

where s and b are the number of signal and background events, respectively, σ_b is the total uncertainty on the background, and b_0 is defined as:

$$b_0 = \frac{1}{2}\left(b - \sigma_b^2 + \sqrt{(b-\sigma_b^2)^2 + 4(s+b)\sigma_b^2}\right) \tag{7.2}$$

In the case where the backround is known precisely (i.e. $\sigma_b = 0$), Equation 7.1 simplifies to

$$Z = \sqrt{2\left(b\big[(1+s/b)\ln(1+s/b) - s/b\big]\right)} \tag{7.3}$$

which further reduces to the familiar $Z = s/\sqrt{b}$ for the case when $s << b$.

7.5.2 Inputs to the optimization

In order to train the RGS, signal and background samples were prepared from events passing the event selection outlined in Table 7.1 up through the b-jet veto. The signal sample was chosen to be the longitudinally polarized $W^{\pm}W^{\pm}jj$ EWK events, and the transverse and mixed polarizations were treated as background along with $W^{\pm}W^{\pm}jj$ events from QCD interactions and the traditional backgrounds listed in Section 7.3. Splitting the inclusive $W^{\pm}W^{\pm}jj$ EWK events by polarization allows the optimization to favor the longitunally polarized events as much as possible, even though they both contribute to the EWK signal.

The following variables were chosen for optimization:

- Leading lepton p_{T}
- Dilepton invariant mass (m_{ll})
- Leading and subleading jet p_{T}
- Dijet invariant mass (m_{jj})
- Lepton-jet centrality (ζ)

Subleading lepton p_{T} was omitted as it is desirable to keep the cut value as low as possible due to its sensitivity to the longitudinal polarization (as discussed in Section 7.1.1). Additionally, the dijet separation $\Delta\eta_{jj}$ was included in the optimization originally, however it was dropped from the list due to the cut value being motivated by differences between EWK and QCD produced $W^{\pm}W^{\pm}jj$ events.

Two additional constraints were imposed when selecting the optimal cut point:

1. At least 1000 signal events must survive in order to prevent the optimization from being too aggressive and unnecssarily reducing signal statistics.
2. The dijet invariant mass may only vary within a 50 GeV range of the default value (from 450-550 GeV) due to the cut being physically motivated by the VBS event topology (TODO: reference where this is discussed in the 13TeV section).

Lastly, the decision was made to use calculate the signal significance without taking into account the uncertainty of the background using Equation 7.3. This was due to the fact that the statistical uncertainties of the fake electron and charge-misID backgrounds were quite large, and if Equation 7.1 were used instead, the optimization would cut unreasonably hard against these backgrounds. Since Monte Carlo statistics is not expected to be a limiting factor when this analysis is performed at the HL-LHC, it is more realistic to simply ignore these large statistical uncertainties for the purpose of the selection optimization.

7.5.3 Results of the optimization

Ultimately, the random grid was constructed from over 38,000 LL-polarized $W^{\pm}W^{\pm}jj$ events in the variables listed above. After applying the constraints, an optimal cut point was chosen which reduced the total background from 9900 to 2310 while reducing the signal from 3489 to 2958. This corresponds to an increase in signal significance from $Z = 33.26$ to $Z = 52.63$ as calculated by Equation 7.3. The updates to the event selection are listed in Table 7.2.

The large reduction in the background is primarily a result of the increase in the leading and subleading jet p_{T} from 30 GeV to 90 GeV and 45 GeV, respectively. As can be seen in Figure 7.7, this increase removes a significant portion of the backgrounds from jets faking electrons and charge mis-ID. Additionally, the loosening of the lepton-jet centrality cut ζ allows more signal events to survive the event selection (see Figure 7.9). Other changes to the event selection are minor and do not individually have a large impact on the signal or background yields.

The full event yields after optimization as well as the cross section measurement are detailed alongside those using the default selection in Section 7.6.

TODO: It's a bit awkward to reference the results of the default/optimized before they're properly presented. Maybe move the sections around? not sure...

Selection requirement	Selection value
Lepton kinematics	$p_{\mathrm{T}} > 28$ GeV (leading lepton only)
Jet kinematics	$p_{\mathrm{T}} > 90$ GeV (leading jet) $p_{\mathrm{T}} > 45$ GeV (subleading jet)
Dilepton mass	$m_{ll} > 28$ GeV
Dijet mass	$m_{jj} > 520$ GeV
Lepton-jet centrality	$\zeta > -0.5$

Table 7.2: Updates to the $W^{\pm}W^{\pm}jj$ event selection criteria after optimization. Cuts not listed remain unchanged from the default selection in Table 7.1.

7.6 Results

7.6.1 Event yields

7.6.2 Uncertainties

7.6.3 Cross section measurement

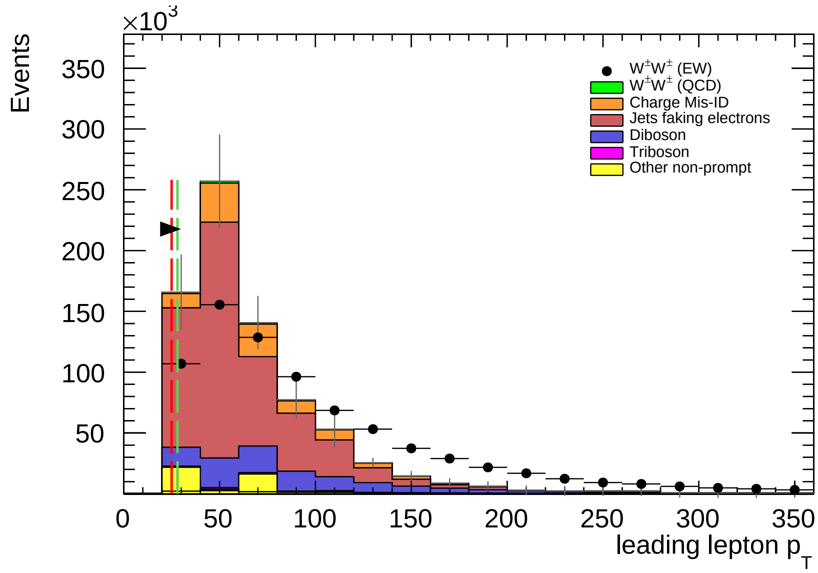

Figure 7.5: Leading lepton p_{T} distribution. The default and optimized cuts are represented by the red and green dashed lines, respectively. The $W^{\pm}W^{\pm}jj$ EWK signal (black points) is normalized to the same area as the sum of the backgrounds (colored histogram). TODO: Move to appendix or omit

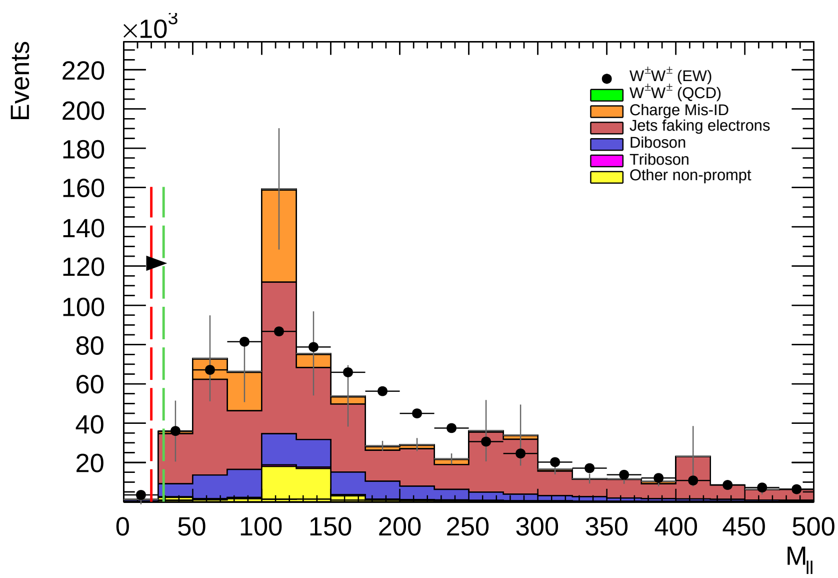

Figure 7.6: Dilepton invariant mass distribution. The default and optimized cuts are represented by the red and green dashed lines, respectively. The $W^{\pm}W^{\pm}jj$ EWK signal (black points) is normalized to the same area as the sum of the backgrounds (colored histogram). TODO: Move to appendix or omit

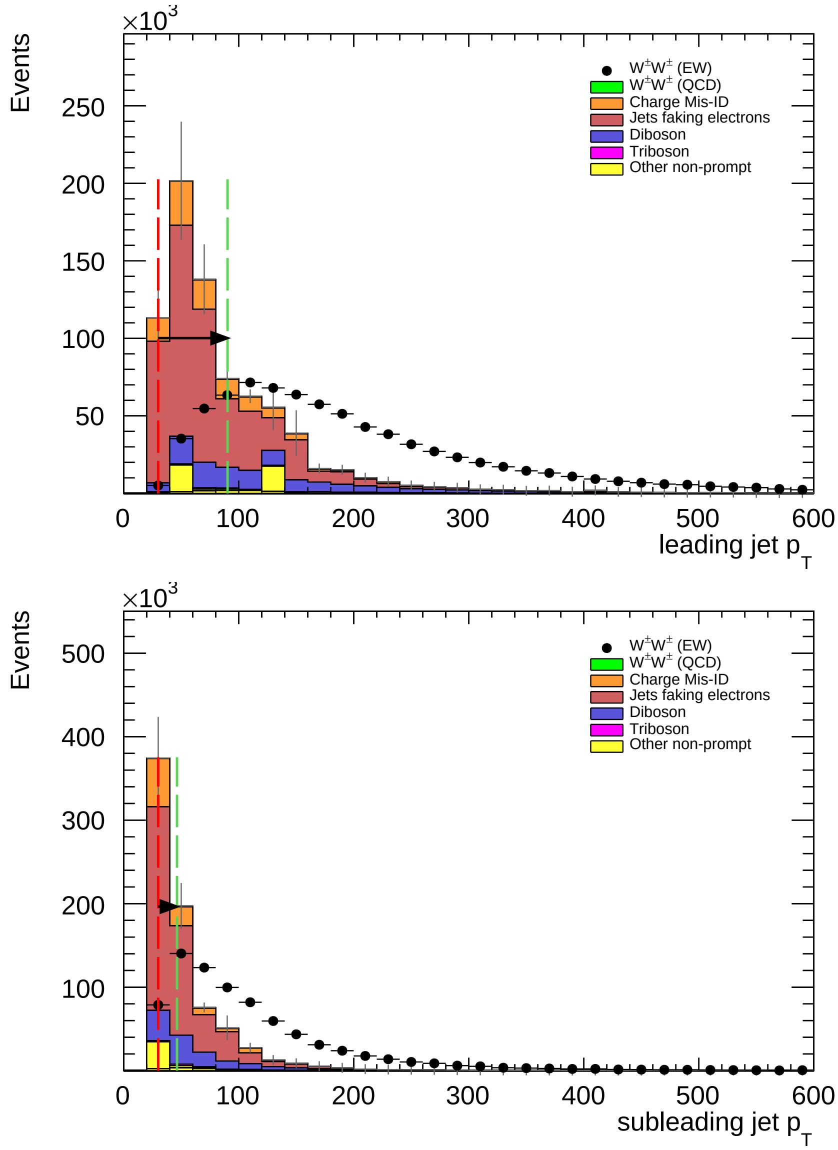

Figure 7.7: Leading (top) and subleading (bottom) jet p_{T} distributions. The default and optimized cuts are represented by the red and green dashed lines, respectively. The $W^{\pm}W^{\pm}jj$ EWK signal (black points) is normalized to the same area as the sum of the backgrounds (colored histogram).

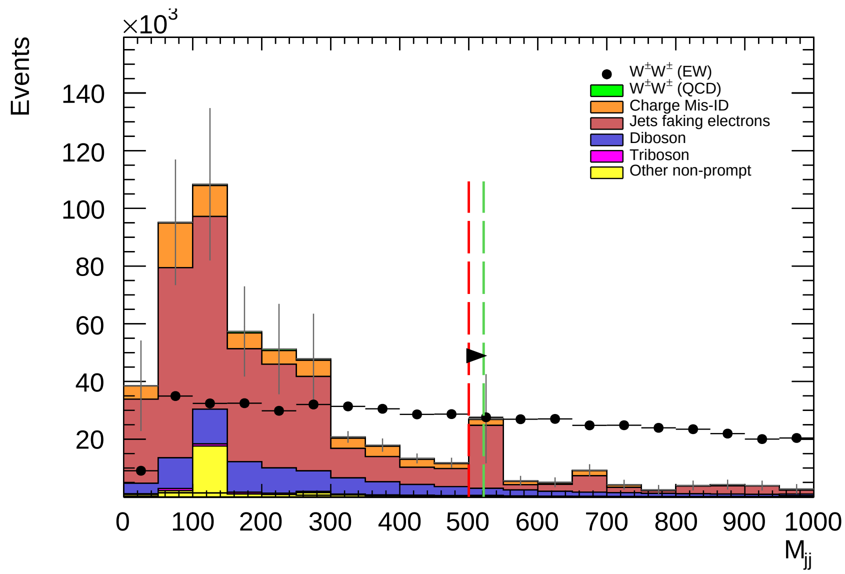

Figure 7.8: Dijet invariant mass distribution. The default and optimized cuts are represented by the red and green dashed lines, respectively. The $W^{\pm}W^{\pm}jj$ EWK signal (black points) is normalized to the same area as the sum of the backgrounds (colored histogram). TODO: Move to appendix or omit

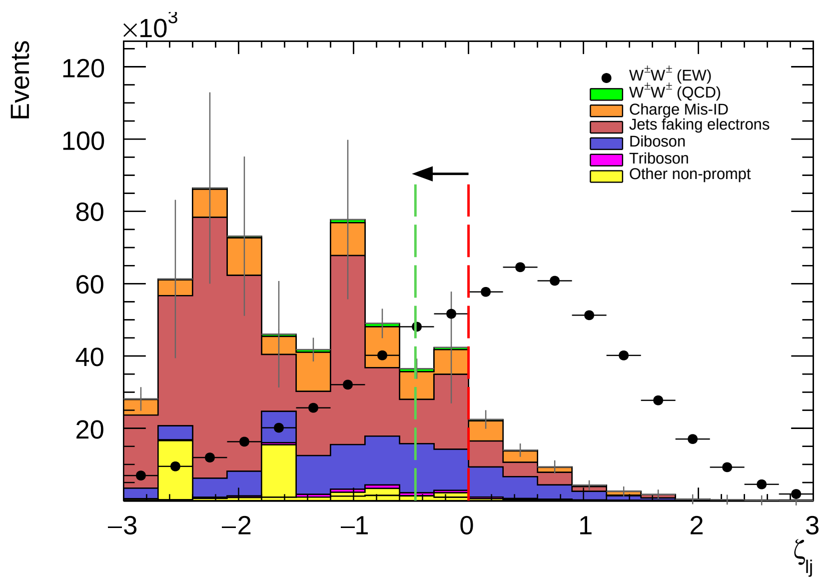

Figure 7.9: Lepton-jet centrality distribution. The default and optimized cuts are represented by the red and green dashed lines, respectively. The $W^{\pm}W^{\pm}jj$ EWK signal (black points) is normalized to the same area as the sum of the backgrounds (colored histogram).

Chapter 8

Conclusion

Here's where you wrap it up.

Looking Ahead

Here's an example of how to have an "informal subsection".

Bibliography

[1] K. J. Potamianos, W. K. Di Clemente, M.-A. Pleier, C. A. Lee, J. I. Kroll, S. Yacoob, and M. Leigh, *Prospects for the measurement of the $W^{\pm}W^{\pm}$ scattering cross section and extraction of the longitudinal scattering component in pp collisions at the High-Luminosity LHC with the ATLAS experiment.*, Tech. Rep. ATL-COM-PHYS-2018-1479, CERN, Geneva, Oct, 2018. https://cds.cern.ch/record/2644264. (document), 7.1, 7.2

[2] S. L. Glashow, *The Renormalizability of Vector Meson Interactions*, Nucl. Phys. **10** (1959) 107–117. 2.2

[3] A. Salam and J. C. Ward, *Weak and Electromagnetic Interactions*, Nuovo Cimento **11** (1959) 568–577. 2.2

[4] L. R. Evans and P. Bryant, *LHC Machine*, JINST **3** (2008) S08001. https://cds.cern.ch/record/1129806. This report is an abridged version of the LHC Design Report (CERN-2004-003). 3.1

[5] ATLAS Collaboration, *The ATLAS Experiment at the CERN Large Hadron Collider*, JINST **3** (2008) S08003. 3.1

[6] ATLAS Collaboration Collaboration, *Alignment of the ATLAS Inner Detector Tracking System with 2010 LHC proton-proton collisions at $\sqrt{s} = 7\ TeV$*, Tech. Rep. ATLAS-CONF-2011-012, CERN, Geneva, Mar, 2011. https://cds.cern.ch/record/1334582. 4

[7] R. Steerenberg, *LHC Report: Another run is over and LS2 has just begun...*, https://home.cern/news/news/accelerators/lhc-report-another-run-over-and-ls2-has-just-begun, 2018. Accessed: 2018-12-14. 7

[8] *Letter of Intent for the Phase-I Upgrade of the ATLAS Experiment*, Tech. Rep. CERN-LHCC-2011-012. LHCC-I-020, CERN, Geneva, Nov, 2011. http://cds.cern.ch/record/1402470. 7

[9] G. Apollinari, I. Bjar Alonso, O. Brning, M. Lamont, and L. Rossi, *High-Luminosity Large Hadron Collider (HL-LHC): Preliminary Design Report.* CERN Yellow Reports: Monographs. CERN, Geneva, 2015. https://cds.cern.ch/record/2116337. 7

[10] ATLAS Collaboration Collaboration, ATLAS Collaboration, *ATLAS Phase-II Upgrade Scoping Document*, Cern-lhcc-2015-020, Geneva, Sep, 2015. http://cds.cern.ch/record/2055248. 7

[11] D. Espriu and B. Yencho, *Longitudinal WW scattering in light of the "Higgs boson" discovery*, Phys. Rev. D **87** (2013) 055017, arXiv:1212.4158 [hep-ph]. 7, 7.1

[12] ATLAS Collaboration Collaboration, *Prospects for the measurement of the $W^{\pm}W^{\pm}$ scattering cross section and extraction of the longitudinal scattering component in pp collisions at the High-Luminosity LHC with the ATLAS experiment*, Tech. Rep. ATL-PHYS-PUB-2018-052, CERN, Geneva, Dec, 2018. http://cds.cern.ch/record/2652447. 7

[13] ATLAS Collaboration Collaboration, *Studies on the impact of an extended Inner Detector tracker and a forward muon tagger on $W^{\pm}W^{\pm}$ scattering in pp collisions at the High-Luminosity LHC with the ATLAS experiment*, Tech. Rep. ATL-PHYS-PUB-2017-023, CERN, Geneva, Dec, 2017. https://cds.cern.ch/record/2298958. 7, 7.4

[14] B. W. Lee, C. Quigg, and H. B. Thacker, *The Strength of Weak Interactions at Very High-Energies and the Higgs Boson Mass*, Phys. Rev. Lett. **38** (1977) 883–885. 7.1

[15] J. Alwall, R. Frederix, S. Frixione, V. Hirschi, F. Maltoni, O. Mattelaer, H. S. Shao, T. Stelzer, P. Torrielli, and M. Zaro, *The automated computation of tree-level and next-to-leading order differential cross sections, and their matching to parton shower simulations*, JHEP **07** (2014) 079, arXiv:1405.0301 [hep-ph]. 7.2

[16] R. D. Ball et al., *Parton distributions for the LHC Run II*, JHEP **04** (2015) 040, arXiv:1410.8849 [hep-ph]. 7.2

[17] T. Sjöstrand, S. Ask, J. R. Christiansen, R. Corke, N. Desai, P. Ilten, S. Mrenna, S. Prestel, C. O. Rasmussen, and P. Z. Skands, *An Introduction to PYTHIA 8.2*, Comput. Phys. Commun. **191** (2015) 159–177, arXiv:1410.3012 [hep-ph]. 7.2

[18] T. Gleisberg et al., *Event generation with SHERPA 1.1*, JHEP **02** (2009) 007, arXiv:0811.4622 [hep-ph]. 7.2

[19] S. Schumann and F. Krauss, *A parton shower algorithm based on Catani-Seymour dipole factorization*, JHEP **03** (2008) 038, arXiv:0709.1027 [hep-ph]. 7.2

[20] S. Höche, F. Krauss, S. Schumann, and F. Siegert, *QCD matrix elements and truncated showers*, JHEP **05** (2009) 053, arXiv:0903.1219 [hep-ph]. 7.2

[21] S. Alioli, P. Nason, C. Oleari, and E. Re, *A general framework for implementing NLO calculations in shower Monte Carlo programs: the POWHEG BOX*, JHEP **06** (2010) 043, arXiv:1002.2581 [hep-ph]. 7.2

[22] H.-L. Lai, M. Guzzi, J. Huston, Z. Li, P. M. Nadolsky, J. Pumplin, and C. P. Yuan, *New parton distributions for collider physics*, Phys. Rev. D **82** (2010) 074024, arXiv:1007.2241 [hep-ph]. 7.2

[23] S. Agostinelli et al., *GEANT4 - a simulation toolkit*, Nucl. Instrum. Meth. **A506** (2003) 250–303. 7.2

[24] P. C. Bhat, H. B. Prosper, S. Sekmen, and C. Stewart, *Optimizing Event Selection with the Random Grid Search*, Comput. Phys. Commun. **2**28 (2018) 245–257, arXiv:1706.09907 [hep-ph]. 7.5.1

[25] G. Cowan, K. Cranmer, E. Gross, and O. Vitells, *Asymptotic formulae for likelihood-based tests of new physics*, Eur. Phys. J. **C**71 (2011) 1554, arXiv:1007.1727 [physics.data-an]. [Erratum: Eur. Phys. J.C73,2501(2013)]. 7.5.1